NANO LETTERS
Letter
Cite This: Nano Lett. 2018, 18, 4611−4617
pubs.acs.org/NanoLett

New Deformation-Induced Nanostructure in Silicon

Bo Wang,[†,‡,⊥] Zhenyu Zhang,[*,†,⊥] Keke Chang,[‡,⊥] Junfeng Cui,[†,‡] Andreas Rosenkranz,[§] Jinhong Yu,[‡] Cheng-Te Lin,[‡] Guoxin Chen,[‡] Ketao Zang,[∥] Jun Luo,[∥] Nan Jiang,[*,‡] and Dongming Guo[†]

[†]Key Laboratory for Precision and Non-Traditional Machining Technology of Ministry of Education, Dalian University of Technology, Dalian 116024, China

[‡]Key Laboratory of Marine Materials and Related Technologies, Ningbo Institute of Materials Technology and Engineering, Chinese Academy of Sciences, Ningbo 315201, China

[§]Department of Chemical Engineering, Biotechnology and Materials, Universidad de Chile, Avenido Tupper 2069, Santiago Chile

[∥]Center for Electron Microscopy, Institute for New Energy Materials and Low-Carbon Technologies, School of Materials Science and Engineering, Tianjin University of Technology, Tianjin 300384, China

Downloaded via UNIV DE CHILE on August 17, 2018 at 13:55:58 (UTC).
See https://pubs.acs.org/sharingguidelines for options on how to legitimately share published articles.

ABSTRACT: Nanostructures in silicon (Si) induced by phase transformations have been investigated during the past 50 years. Performances of nanostructures are improved compared to that of bulk counterparts. Nevertheless, the confinement and loading conditions are insufficient to machine and fabricate high-performance devices. As a consequence, nanostructures fabricated by nanoscale deformation at loading speeds of m/s have not been demonstrated yet. In this study, grinding or scratching at a speed of 40.2 m/s was performed on a custom-made setup by an especially designed diamond tip (calculated stress under the diamond tip in the order of 5.11 GPa). This leads to a novel approach for the fabrication of nanostructures by nanoscale deformation at loading speeds of m/s. A new deformation-induced nanostructure was observed by transmission electron microscopy (TEM), consisting of an amorphous phase, a new tetragonal phase, slip bands, twinning superlattices, and a single crystal. The formation mechanism of the new phase was elucidated by ab initio simulations at shear stress of about 2.16 GPa. This approach opens a new route for the fabrication of nanostructures by nanoscale deformation at speeds of m/s. Our findings provide new insights for potential applications in transistors, integrated circuits, diodes, solar cells, and energy storage systems.

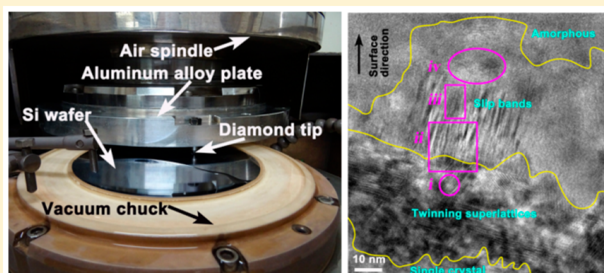

KEYWORDS: *Nanostructure, Si, deformation, transmission electron microscopy, stress*

Silicon (Si) dominates consumer electronics,[1] solar cells,[2] photovoltaic industry,[3] semiconductor devices, and becomes the foundation of electronics industry, which can be considered as the largest industry in the world.[4] Crystalline and amorphous forms are the principal states of Si,[5−7] and nanostructures by transformation between both states greatly influence mechanical, optical, electrical, and electrochemical properties of high performance devices.[1−3,8−14] In this regard, nanostructures by means of phase transformation of Si have been studied for over half a century[15,16] by diamond anvil cells,[14,17] compression,[7,9,18] scratching,[19,20] nanoindentation,[21] nanoscratching[22] and bending.[18,23−25] However, bulk Si absorbs and emits photons weakly, because of the second-order momentum-conserving processes inefficiently.[1] Because of the paucity of defects and the large surface-to-volume ratio,[26] Si nanostructures have revealed superior[12,17,27,28] mechanical,[23,24] optical,[1] electrical,[2] and electrochemical[11,28] properties, compared to the bulk counterparts. For instance, thin film solar cells involving nanostructures are flexible and transparent,[2] thus leading to a material reduction by 150−200 times compared to bulk Si-wafer based solar cells.[29]

Cutting speeds vary from 15 to 18 m/s in machining and fabricating high-performance Si devices.[21] This is obviously different from present confinement and loading conditions used in hydrostatic pressure,[14,17] nanoindentation,[21] nanoscratching,[22] and bending.[23,24] Cutting speeds are 10 mm/s[19] and 2.67 mm/s[20] in scratching experiments to characterize the microstructural changes in Si. However, the work is at the micrometer level instead of the nanoscale. A scratching speed of 0.4 μm/s is used in nanoscratching,[22] which is 7 orders of magnitude lower than m/s applied in machining and fabricating. Indenting speeds of nanoindentation are 8 nm/s[21] and 60 nm/s[30] in air and in situ transmission electron microscopy (TEM) respectively. In situ TEM nanomechanical tests have loading speeds of 10−30 nm/s in bending,[23] 2−4 nm/s in compression,[7,9] and 5 nm/s in tension,[31] which are 8−9 orders of magnitude lower compared to conventional machining and fabricating. As a result, nanostructures induced by nanoscale deformation at loading speeds of m/s have not been demonstrated yet. It is highly

Received: May 10, 2018
Revised: June 8, 2018
Published: June 18, 2018

ACS Publications © 2018 American Chemical Society

DOI: 10.1021/acs.nanolett.8b01910
Nano Lett. 2018, 18, 4611−4617

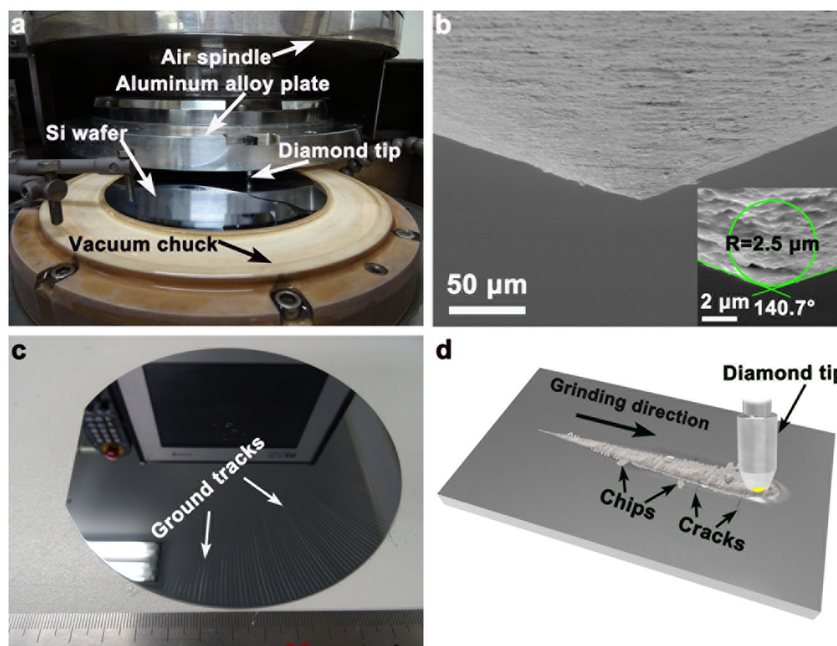

Figure 1. (a) Photograph of a developed setup performing grinding induced by (b) (SEM image) a single diamond tip developed, (c) photograph of a ground Si wafer, and (d) schematic diagram under grinding at the onset of chip and crack formations.

Table 1. Summary of the Grinding Conditions Performed by a Specially Designed Single Diamond Tip

			at the onset of chip formation				
diamond tip (shape)	included angle (deg)	tip radius (μm)	width (nm)	depth (nm)	wheel speed (m/s)	table speed (rpm)	feed rate of diamond tip (μm/min)
conical	140.7	2.5	456	33	40.2	120	10

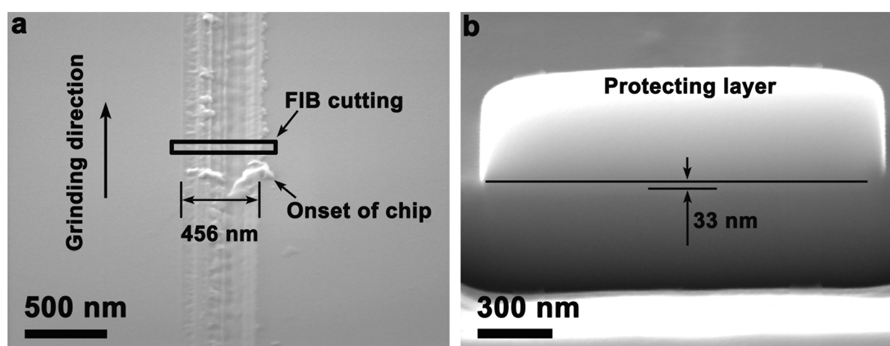

Figure 2. SEM images of (a) the surface after grinding and (b) cross-sectional view of the surfaces marked by a black square in (a) at the onset of chip formation.

desirable to machine and fabricate nanostructures of Si at speeds of m/s for potential applications in integrated circuits (IC), diodes, transistors, solar cells, and energy storage systems.[12]

Transformation pathway in Si is dramatically affected by stress-induced confinement and loading conditions. In nanoindentation, diamond cubic (Si-I) transforms to β-Sn (Si-II) during loading[7,9,22] under a stress of approximately 11.7 GPa.[1] During unloading, β-Sn turns into an amorphous phase and/or a mixture of high pressure Si-III and Si-XII phases.[9,22] In core/shell configuration, diamond cubic Si directly converts to an amorphous phase under compression at stress of 8.5 GPa, without involving any intermediate crystalline phase.[7] Under compression, diamond cubic transforms to an intermediate diamond hexagonal structure at ~18 GPa, and then changes to an amorphous phase.[9] In diamond anvil cells, the metallic β-Sn experiences a transformation to Si-XI phase at 13.2 GPa. At a higher pressure of 15.4 GPa, Si-XI transforms to Si-V, followed by a transformation at ~38 GPa. At a pressure of 42 GPa, Si-VI undergoes a transformation to Si-VII. Finally, Si-VII transforms into Si-X at ~79 GPa.[1] All the above-mentioned phase transformations occur via nanoscale deformation at loading speeds of nm/s or μm/s. It is unclear what kind of nanostructure is induced via nanoscale deformation under loading speeds of m/s. Moreover, fundamental mechanisms for the formation of nanostructure are not understood.

In this research, grinding or scratching at a speed of 40.2 m/s was conducted on a custom-built setup using a specially designed diamond tip. A new deformation-induced nanostruc-

DOI: 10.1021/acs.nanolett.8b01910
Nano Lett. 2018, 18, 4611−4617

ture was observed by TEM after grinding. Ab initio simulations and theoretical calculations were carried out to elucidate the formation mechanism of the nanostructure.

Results and Discussion. A setup was developed to perform grinding induced by a specially designed single diamond tip, as illustrated in Figure 1a. The diamond tip has a conical shape with a tip radius of 2.5 μm and an included angle of 140.7°, as depicted in Figure 1b. Well separated ground tracks are present on a Si wafer (Figure 1c). The chip formation induced by grinding using a single diamond tip is shown in Figure 1d. All grinding conditions are summarized in Table 1. The grinding speed was 40.2 m/s, and the feed rate of the diamond tip was 10 μm/min. Figure 2 shows the ground surface with a pronounced grinding mark as well as cross-sectional view at the onset of chip formation, whose width (Figure 2a) and depth (Figure 2b) are 456 and 33 nm, respectively.

Figure 3 shows a cross-sectional TEM image of the nanostructure at the onset of chip formation. The nanostructure

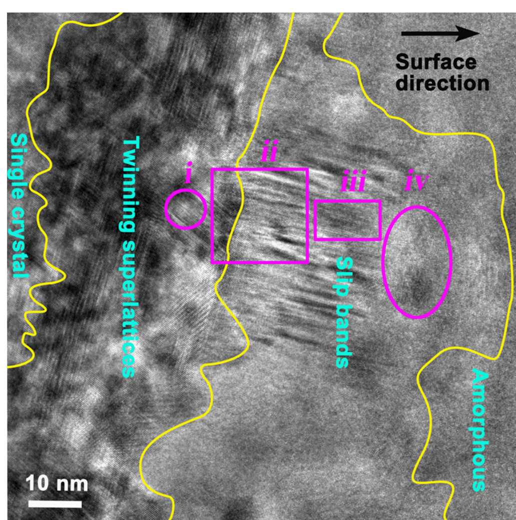

Figure 3. Cross-sectional TEM image of the nanostructure at the onset of chip formation.

consists of an amorphous phase at the topmost, followed by a new tetragonal phase, slip bands, twinning superlattices and a single crystal at the downmost. The thickness of twinning superlattices is approximately 40 nm.

A high-resolution TEM (HRTEM) image of the nanostructure of the twinning superlattices and its fast Fourier transformation (FFT) are shown in Figure 4a,b, respectively. In reciprocal space, distances between {111} planes are divided equally into three parts, indicating the characteristics of twinning superlattices. Schematic diagram of the twinning superlattices is depicted in Figure 4c.

Figure 5 illustrates the TEM images of two different regions marked by a pink square (ii) and rectangle (iii), respectively in Figure 3. A structure having short-range order is observed at the transition part between twinning superlattices and slip bands, as shown in Figure 5a. Edge dislocations form the boundary of slip bands. A rotation angle of 21.8° can be found between the $(11\bar{1})$ of twinning superlattices and {111} planes in slip bands. In Figure 5a, the thickness of slip bands varies from 3 to 4 nm. The thickness of slip bands turns larger ranging from 4 to 10 nm in Figure 5b. An amorphous phase is observed in slip bands.

Figure 6 displays the TEM image in the area marked by a pink ellipse (iv) in Figure 3. A nanocrystalline, an amorphous and a

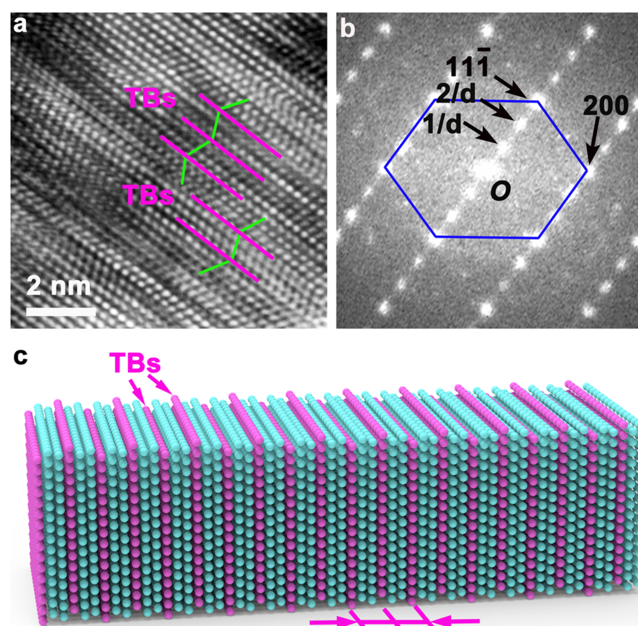

Figure 4. TEM image of (a) twinning superlattices in the area marked by a pink circle (i) in Figure 3, as well as (b) the corresponding FFT pattern, and (c) its schematic diagram.

new tetragonal phase are found in Figure 6a. It is intriguing to observe a new tetragonal phase in Si after grinding induced by a single diamond tip. After FFT in the area of the new phase, four diffraction spots occur as can be seen in Figure 6b. The angle between adjacent spots is 90°, and the distance between each spot to the central one is equal. With inverse FFT (IFFT), an HRTEM image of the tetragonal phase is illustrated in Figure 6c. A strip is drawn by two curved yellow lines, which can be affiliated to diamond cubic Si-I phase. Edge dislocations distribute on two curved yellow lines, separating the Si-I phase from tetragonal phase. A bending pink line is marked by five parallel pink arrows, indicating a slip line from Si-I phase to tetragonal phase. The distance between two adjacent planes in the tetragonal phase is 0.302 and 0.3025 nm in horizontal and vertical direction, respectively, as measured in Figure 6d. This is consistent with the characteristics of diffraction spots presented in Figure 6b. Hence, the tetragonal phase belongs to a tetragonal crystal system.

The specially designed diamond tip had a tip radius of 2.5 μm, as listed in Table 1, which is similar compared to grits of a diamond wheel with a mesh size of 3000. The diamond wheel is commonly used in ultraprecision grinding in semiconductor and microelectronics industries. The onset of chip formation is the start of material removal in grinding (Figure 2), which is significant for the ultraprecision machining and fabricating for high performance devices. At the onset of chip formation, the force and depth of cut are difficult to measure due to the lack of in situ measurement techniques for the force and the depth, which is typically in the nanoscale. Thus, it is important to calculate the force and depth of cut to control them on the diamond tip. This is necessary to develop novel ultraprecision machining techniques and setups, as well as for high performance devices. The normal force, F_n is calculated as[32]

$$F_n = \frac{\pi H a^2}{\lambda^2} \quad (1)$$

DOI: 10.1021/acs.nanolett.8b01910
Nano Lett. 2018, 18, 4611−4617

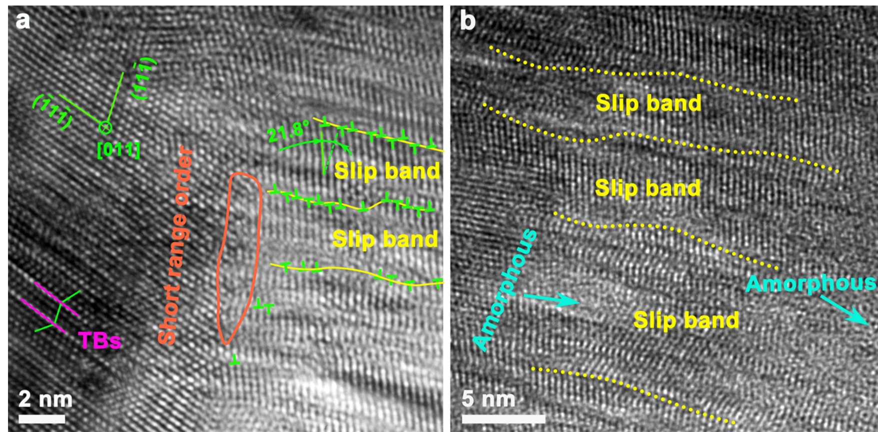

Figure 5. TEM images in the area marked by (a) a pink square (ii) and (b) rectangle (iii), respectively in Figure 3. The right side is toward the surface direction.

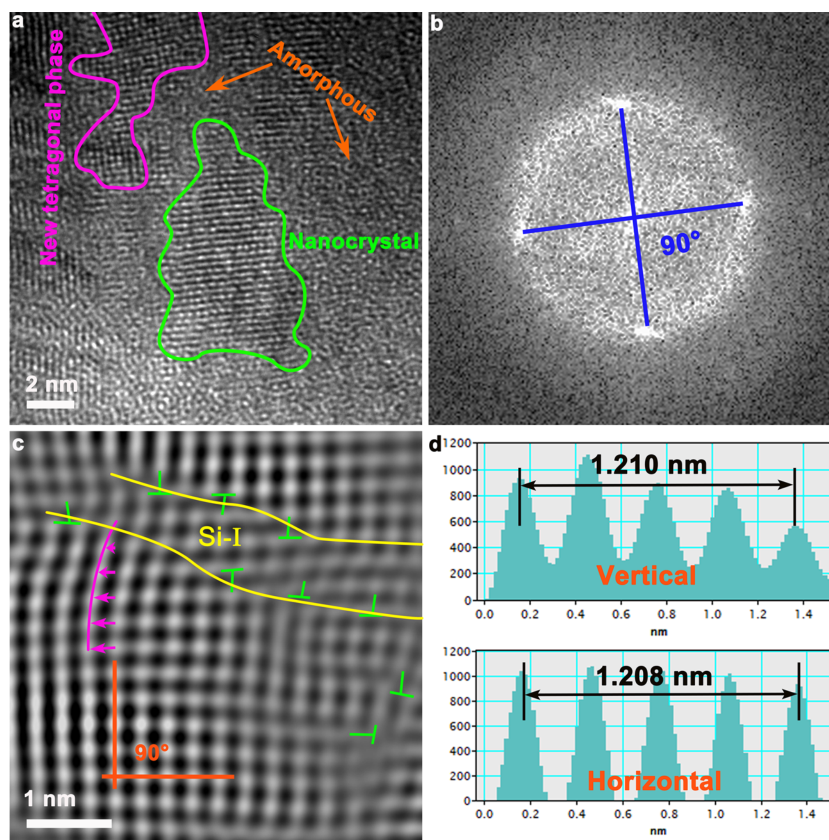

Figure 6. (a) TEM image in the area marked by a pink ellipse (iv) in Figure 3, (b) FFT pattern, (c) IFFT image, and (d) distances of four planes for the new tetragonal phase in (a). The right side is toward the surface direction.

where H is the hardness, a is a half of width, and λ is a dimensionless parameter. The hardness of Si(100) is 13.2 GPa.[2] λ is 1 for an indenter.[1] The plastic radius, p_r can be expressed as[33]

$$p_r = a\left[\frac{3(1-2\nu)}{5-4\nu} + \frac{2\sqrt{3}}{\pi(5-4\nu)}\frac{E}{\sigma_y}\cot\alpha\right]^{0.5} \tag{2}$$

where ν is the Poisson's ratio, E is the elastic modulus, σ_y is the yield strength, and α is the half-included angle. ν and E of the Si(100) are 0.3 and 150.2 GPa, respectively.[33] σ_y is presented as[34]

$$\sigma_y = \frac{H}{2.8} \tag{3}$$

The lateral force, F_l is given as

$$F_l = \mu F_n \tag{4}$$

where μ is the friction coefficient, which is 0.08 between a diamond tip and a Si(100) wafer.[35] The depth of cut, h, can be described as[36]

$$h = \left[\frac{3F_n}{4E^*\sqrt{R}}\right]^{2/3} \tag{5}$$

DOI: 10.1021/acs.nanolett.8b01910
Nano Lett. 2018, 18, 4611−4617

where E^* is the effective indentation modulus and R is the tip radius. E^* is given as[36]

$$\frac{1}{E^*} = \frac{1 - \nu_s^2}{E_s} + \frac{1 - \nu_i^2}{E_i} \tag{6}$$

E_s and ν_s are the Young's modulus and Poisson's ratio of Si(100) wafers, respectively, and E_i and ν_i are those of the diamond tip. E_i and ν_i are 1141 GPa and 0.07, respectively.[36] Calculated forces and plastic sizes are summarized in Table 2. The calculated depth of cut is about 39 nm at the onset of chip formation, which agrees well with measured value by FIB of about 33 nm. The calculated normal stress is about 5.11 GPa at the onset of chip formation.

Table 2. Calculated Forces and Plastic Sizes under Grinding at the Onset of Chip Formation

	at the onset of chip formation				
diamond tip (shape)	F_n (μN)	F_l (μN)	p_r (nm)	h (nm)	normal stress (GPa)
conical	2155	172	434	39	5.11

To elucidate the formation mechanism of the new tetragonal phase, ab initio calculations were performed, as shown in Figure 7. Diamond cubic Si-I phase transforms from face-centered cubic (fcc) structure to the new tetragonal phase under compression induced by grinding, as illustrated from Figure 7a−c. The transformation was conducted by the slips of atoms in the $(11\bar{1})$ plane along the $[1\bar{1}2]$ orientation (Figure 7d). The calculated Si—Si bond length of the original structure is 2.351 Å, which is in good agreement with previous reports (2.352 Å).[12] After compression, the Si—Si bond length at the (110) plane is 2.390 Å, while the bond length between one Si atom at the (110) plane and the other at the (220) is 2.183 Å. The calculated migration energy of one Si atom is 0.38 eV (Figure 7e), whereas the Si−Si bond energy is 2 eV. Therefore, it can be confirmed that no Si−Si bond is broken. The calculated average force is 0.276 nN to move a Si atom (Figure 7f), which is reasonable compared to that required force to move a cobalt (Co) atom on a Pt surface (0.21 nN).[37] In the $(11\bar{1})$ plane, a plane density of atoms is 7.8296×10^{18} m^{-2}, and the shear stress is about 2.16 GPa to form the new tetragonal phase from the fcc structure. Peierls stress, τ_p, is determined as[38]

$$\tau_P = \frac{2G}{1 - \nu} \exp\left(-\frac{2\pi}{1 - \nu}\frac{d}{b}\right) \tag{7}$$

where G is the shear modulus, d is the spacing of a glide plane, and b is the magnitude of Burgers vector. G is derived from the elastic modulus as[39]

$$G = \frac{E}{2(1 + \nu)} \tag{8}$$

The lattice constant of Si is 5.431 Å.[12] The elastic modulus of $\{111\}\langle 112\rangle$ is 169.2 GPa,[33] and the Poisson's ratio[40] of $\langle 111\rangle\langle 112\rangle$ is 0.182. d and S_b for shuffle movement in Si are 2.35 and 3.84 Å, respectively.[41] The Peierls stress is 1.59 GPa, which is in good agreement with 2.16 GPa calculated by ab initio simulations.

The grinding speed was 40.2 m/s at a depth of cut of 33 nm in our experiments. The loading speed is 3−4 and 8−10 orders magnitude higher than those of scratching[19,20] in air and in nanomechanical tests in air and TEM[7,9,21−23,30,31] respectively. Using such high loading speeds, nanomechanical experiments can be regarded as quasi-static loading. This is the substantial difference between our grinding experiments and previous reports. Besides this, there is no material removal occurring in nanoindentation, compression and bending. It is noted that the tip radius of nanoindentation is 50 or 150 nm,[30] which is sharper than 1 μm used in nanoscratching,[22] thus producing intense local stress concentration in the first case. In nanoscratching, pile-ups happen ahead and aside the scratching tip due to the ultralow scratching speed,[22] which makes the confinement

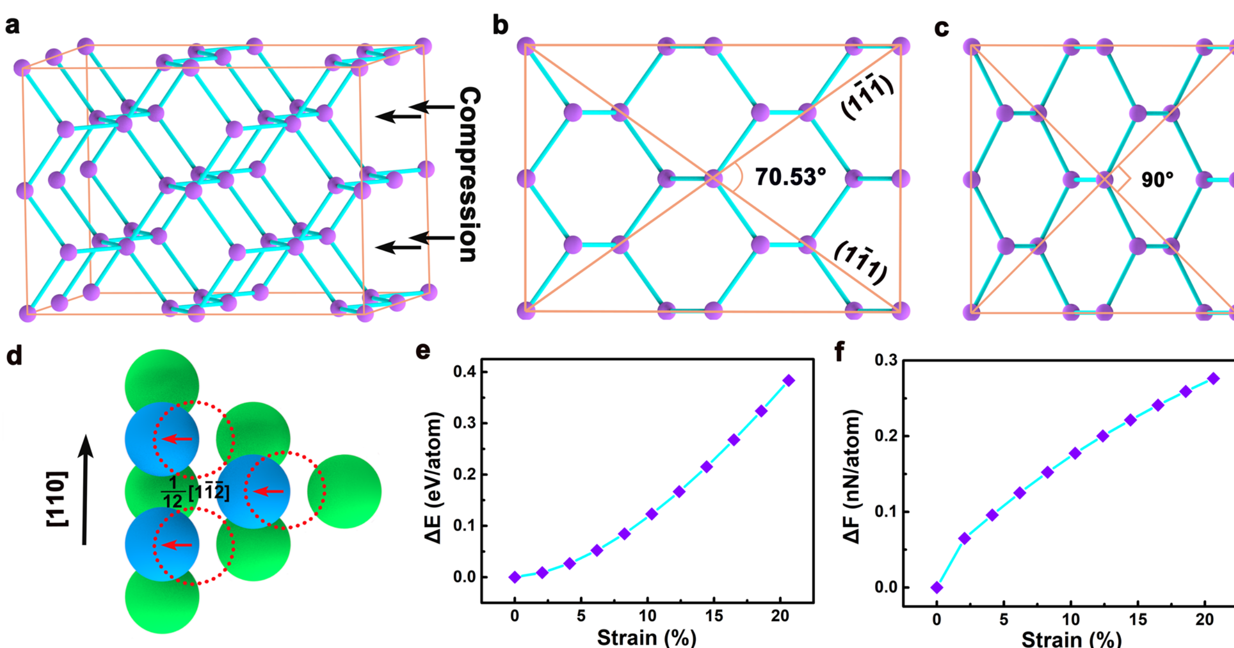

Figure 7. (a) Oblique view of a supercell with 32 atoms, views from ⟨110⟩ orientation prior to (b) and after (c) compression, schematic diagram (d) of atoms slip on {111} planes, and ab initio calculated (e) average migration energy and (f) average force to move a Si atom.

DOI: 10.1021/acs.nanolett.8b01910
Nano Lett. 2018, 18, 4611−4617

effectively. Obvious material removal takes place on the ground surface of Si, as depicted in Figures 1c and 2a. At high loading speeds and in a material removal mode, confinement is ineffective due to a relatively low stress state. Using theoretical calculations, the stress is 5.11 GPa under the diamond tip during grinding, which is lower than 11.7 GPa for the transformation of Si from diamond cubic to Si-II structure.[1] It is distinct from the direct crystalline-to-amorphous transition in the core/shell configuration.[7] Consequently, a new nanostructure induced by nanoscale deformation is found by TEM. The nanostructure includes an amorphous phase, a new tetragonal phase, slip bands, twinning superlattices and a single crystal at the bottom. From ab initio simulation, the new tetragonal phase is formed though slips of atoms in $(11\bar{1})$ plane along $[1\bar{1}\bar{2}]$ orientation at shear stress of 2.16 GPa. This is in a good agreement with 1.59 GPa calculated from Peierls stress.

Conclusions. In summary, grinding was performed on a custom-built setup using a specially designed diamond tip, in which the loading speed was 40.2 m/s at a depth of cut of 33 nm. The calculated stress under the diamond tip was 5.11 GPa during grinding. After grinding, a new nanostructure was observed by TEM with an amorphous phase at the topmost, followed by a new tetragonal phase, slip bands, twinning superlattices and a single crystal at the downmost. The tetragonal phase is formed by slips of atoms in $\{111\}$ along $\langle 112\rangle$ orientation at shear stress of 2.16 GPa, which is simulated by ab initio calculations. This is consistent with the prediction of the Peierls stress. The approach used in our work offers a new way to machine and fabricate nanostructures in Si by nanoscale deformation, which will be very useful for applications in IC, solar cells, energy storage systems, and so forth.

Experimental Section. A single diamond tip was developed from a diamond grain imported from South Africa. First, the diamond grain was put in a hole at one end of a 45 carbon steel lever. Then the hole was filled with nickel-based powder. The diamond grain was fixed using high-frequency welding. It was ground on a precision grinder by resin bond diamond wheels with mesh sizes of 300, 800, and 3000. A vitrified diamond wheel with a mesh size of 5000 was used to machine the diamond tip at the final grinding process. Finally, mechanical chemical polishing (MCP) was employed to finish the diamond tip by a cast iron plate. Chemical reaction was activated between the diamond tip and cast iron plate by the heat generated during the MCP to finish the diamond tip. An aluminum (Al) alloy plate was designed and manufactured according to the structure of an ultraprecision grinder (Okamoto VG401 MKII, Japan). The diamond tip was fixed in a hole of 320 mm in diameter of the Al alloy plate with a diameter of 336 mm. The Al alloy plate was mounted on the ultraprecision grinder. With this approach, a setup was developed to perform the grinding induced by the developed single diamond tip, inducing a depth of cut in the nanometer range.

Commercial Si(100) wafers (Grinm Advanced Materials Co., Ltd.) with a diameter of 150 mm were used as specimens of 100 nm in flatness after chemical mechanical polishing (CMP). Prior to grinding, the diamond tip was fed manually on the ultraprecision grinder. A subtle ground track was observed when the diamond tip touched a Si wafer. A readout was taken at this location. Then the diamond tip was uplifted for 40 μm. Setting up the readout in the grinder, grinding was started. During grinding, the rotational speeds of spindle and work table were 2399 and 120 rpm, respectively, and the feed rate of spindle was 10 μm/min. Coolant was shut off in grinding to obtain the chips (debris) on the ground surface. The diamond tip was uplifted immediately when reaching the readout. Nanoscale depth of cut was guaranteed by a variation of 150 nm between the runout of spindle for 50 nm and a flatness of a Si wafer for 100 nm. After grinding, the Si wafers were flushed and dried by deionized water and compressed air, respectively.

The diamond tip developed and ground surfaces on Si wafers were characterized by scanning electron microscopy (SEM, Lyra3 Tescan, Czech Republic) equipped with focused ion beam (FIB). The width at the onset of chip formation was measured by SEM, and the depth was cut by FIB and then measured by in situ SEM. TEM samples were prepared using FIB (Auriga, Carl Zeiss, Germany). TEM examinations were performed by an FEI Tecnai F20 microscope operated at an accelerated voltage of 200 kV.

Ab initio calculations were performed using the density-functional theory,[42] as implemented in the Vienna ab initio simulation package (VASP).[1] The generalized gradient approximation (GGA) method[43] was performed with the Blöchl corrections for the total energy.[44] Valence electrons were explicitly treated by projector augmented plane-wave (PAW) potentials.[43] The calculations employed a plane-wave cutoff energy of 310 eV, reciprocal space integration with a Monkhorst−Pack scheme[45] and convergence criterion for the total energy of 0.01 meV. The total energy convergence was tested with respect to the *k*-point grid of $7 \times 7 \times 7$. Various configurations of Si atoms were considered to look for the appropriate structure to simulate the experimental observations. In this work, a supercell of 32 Si atoms were applied with a (110) basal plane. The supercell was compressed along the $\langle 1\bar{1}0\rangle$ direction, which was obtained by moving the atoms stepwise from the initial equilibrium positions toward the $(1\bar{1}0)$ plane. The atoms were migrated for 10 steps in total until reaching the final positions. In each step, the total energy of the supercell was calculated. It was speculated that all the increment of the total energy after movement was induced by compression. Consequently, the average force was acquired to move one Si atom.

■ AUTHOR INFORMATION

Corresponding Authors

*E-mail: zzy@dlut.edu.cn.

*E-mail: jiangnan@nimte.ac.cn.

ORCID

Zhenyu Zhang: 0000-0002-2393-520X

Author Contributions

⊥B.W., Z.Z., and K.C. contributed equally to this work.

Notes

The authors declare no competing financial interest.

■ ACKNOWLEDGMENTS

B.W. is grateful for the valuable discussion with Mr. Zhiduo Liu at Institute of Semiconductors, Chinese Academy of Sciences. Z.Z. would like to acknowledge the nice help from Ms. Rong Wang and Associate Professor Wenyan Yang at Tsinghua University for the measurements and characterization by SEM and FIB on the scratched surfaces on Si. The authors acknowledge the financial support from the Excellent Young Scientists Fund of NSFC (51422502), Science Fund for Creative Research Groups of NSFC (51621064), Changjiang Scholar Program of Chinese Ministry of Education, Program for Creative Talents in University of Liaoning Province (LR2016006), Distinguished Young Scholars for Science and

DOI: 10.1021/acs.nanolett.8b01910
Nano Lett. 2018, 18, 4611−4617

Technology of Dalian City (2016RJ05), the Natural Science Foundation of Jiangsu Province (BK20151190), the Xinghai Science Funds for Distinguished Young Scholars and Thousand Youth Talents at Dalian University of Technology, Science Fund of State Key Laboratory of Tribology, Tsinghua University (SKLTKF17B19), Science Fund of State Key Laboratory of Metastable Materials Science and Technology, Yanshan University (201813), and the Collaborative Innovation Center of Major Machine Manufacturing in Liaoning.

■ REFERENCES

(1) Hannah, D. C.; Yang, J. H.; Podsiadlo, P.; Chan, M. K. Y.; Demortiere, A.; Gosztola, D. J.; Prakapenka, V. B.; Schatz, G. C.; Kortshagen, U.; Schaller, R. D. *Nano Lett.* **2012**, *12*, 4200−4205.
(2) Han, G. F.; Zhang, S.; Boix, P. P.; Wong, L. H.; Sun, L. D.; Lien, S. Y. *Prog. Mater. Sci.* **2017**, *87*, 246−291.
(3) Mann, J. K.; Kurstjens, R.; Pourtois, G.; Gilbert, M.; Dross, F.; Poortmans, J. *Prog. Mater. Sci.* **2013**, *58*, 1361−1387.
(4) Pei, Z. J.; Fisher, G. R.; Liu, J. *Int. J. Mach. Tool. Manu.* **2008**, *48*, 1297−1307.
(5) Deb, S. K.; Wilding, M.; Somayazulu, M.; McMillan, P. F. *Nature* **2001**, *414*, 528−530.
(6) Treacy, M. M. J.; Borisenko, K. B. *Science* **2012**, *335*, 950−953.
(7) Wang, Y. C.; Zhang, W.; Wang, L. Y.; Zhuang, Z.; Ma, E.; Li, J.; Shan, Z. W. *NPG Asia Mater.* **2016**, *8*, e291.
(8) Hannon, J. B.; Hibino, H.; Bartelt, N. C.; Swartzentruber, B. S.; Ogino, T.; Kellogg, G. L. *Nature* **2000**, *405*, 552−554.
(9) He, Y.; Zhong, L.; Fan, F. F.; Wang, C. M.; Zhu, T.; Mao, S. X. *Nat. Nanotechnol.* **2016**, *11*, 866−871.
(10) Gerberich, W. W. *Nat. Nanotechnol.* **2016**, *11*, 841−841.
(11) McDowell, M. T.; Lee, S. W.; Nix, W. D.; Cui, Y. *Adv. Mater.* **2013**, *25*, 4966−4984.
(12) Xu, Z. L.; Liu, X. M.; Luo, Y. S.; Zhou, L. M.; Kim, J. K. *Prog. Mater. Sci.* **2017**, *90*, 1−44.
(13) Martin-Bragado, I.; Borges, R.; Balbuena, J. P.; Jaraiz, M. *Prog. Mater. Sci.* **2018**, *92*, 1−32.
(14) Mcmillan, P. F.; Wilson, M.; Daisenberger, D.; Machon, D. A. *Nat. Mater.* **2005**, *4*, 680−684.
(15) Wentorf, R. H.; Kasper, J. S. *Science* **1963**, *139*, 338−339.
(16) Yin, M. T.; Cohen, M. L. *Phys. Rev. Lett.* **1980**, *45*, 1004−1007.
(17) Wang, Y. J.; Zhang, J. Z.; Wu, J.; Coffer, J. L.; Lin, Z. J.; Sinogeikin, S. V.; Yang, W. G.; Zhao, Y. S. *Nano Lett.* **2008**, *8*, 2891−2895.
(18) Chrobak, D.; Tymiak, N.; Beaber, A.; Ugurlu, O.; Gerberich, W. W.; Nowak, R. *Nat. Nanotechnol.* **2011**, *6*, 480−484.
(19) Minowa, K.; Sumino, K. *Phys. Rev. Lett.* **1992**, *69*, 320−322.
(20) Zarudi, I.; Nguyen, T.; Zhang, L. C. *Appl. Phys. Lett.* **2005**, *86*, 011922.
(21) Yan, J. W.; Takahashi, H.; Tamaki, J.; Gai, X. H.; Harada, H.; Patten, J. *Appl. Phys. Lett.* **2005**, *86*, 181913.
(22) Wu, Y. Q.; Huang, H.; Zou, J.; Zhang, L. C.; Dell, J. M. *Scr. Mater.* **2010**, *63*, 847−850.
(23) Tang, D. M.; Ren, C. L.; Wang, M. S.; Wei, X. L.; Kawamoto, N.; Liu, C.; Bando, Y.; Mitome, M.; Fukata, N.; Golberg, D. *Nano Lett.* **2012**, *12*, 1898−1904.
(24) Wang, L. H.; Zheng, K.; Zhang, Z.; Han, X. D. *Nano Lett.* **2011**, *11*, 2382−2385.
(25) Amato, M.; Kaewmaraya, T.; Zobelli, A.; Palummo, M.; Rurali, R. *Nano Lett.* **2016**, *16*, 5694−5700.
(26) Banerjee, A.; Bernoulli, D.; Zhang, H. T.; Yuen, M. F.; Liu, J. B.; Dong, J. C.; Ding, F.; Lu, J.; Dao, M.; Zhang, W. J.; Lu, Y.; Suresh, S. *Science* **2018**, *360*, 300−302.
(27) Wagner, A. J.; Anderson, C. M.; Trask, J. N.; Cui, L.; Chov, A.; Mkhoyan, K. A.; Kortshagen, U. R. *Nano Lett.* **2013**, *13*, 5735−5739.
(28) Wang, F.; Wu, L. J.; Key, B.; Yang, X. Q.; Grey, C. P.; Zhu, Y. M.; Graetz, J. *Adv. Energy Mater.* **2013**, *3*, 1324−1331.
(29) Sharma, K.; Branca, A.; Illiberi, A.; Tichelaar, F. D.; Creatore, M.; van de Sanden, M. C. M. *Adv. Energy Mater.* **2011**, *1*, 401−406.
(30) Wang, B.; Zhang, Z. Y.; Cui, J. F.; Jiang, N.; Lyu, J. L.; Chen, G. X.; Wang, J.; Liu, Z. D.; Yu, J. H.; Lin, C. T.; Ye, F.; Guo, D. M. *ACS Appl. Mater. Interfaces* **2017**, *9*, 29451−29456.
(31) Zhang, Z. Y.; Cui, J. F.; Wang, B.; Jiang, H. Y.; Chen, G. X.; Yu, J. H.; Lin, C. T.; Tang, C.; Hartmaier, A.; Zhang, J. J.; Luo, J.; Rosenkranz, A.; Jiang, N.; Guo, D. M. *Nanoscale* **2018**, *10*, 6261−6269.
(32) Jing, X. N.; Maiti, S.; Subhash, G. *J. Am. Ceram. Soc.* **2007**, *90*, 885−892.
(33) Ebrahimi, F.; Kalwani, L. *Mater. Sci. Eng., A* **1999**, *268*, 116−126.
(34) Lee, S. H. *Int. J. Mach. Tool. Manu.* **2012**, *61*, 71−79.
(35) Gatzen, H. H.; Beck, M. *Wear* **2003**, *254*, 1122−1126.
(36) Shim, S.; Bei, H.; George, E. P.; Pharr, G. M. *Scr. Mater.* **2008**, *59*, 1095−1098.
(37) Ternes, M.; Lutz, C. P.; Hirjibehedin, C. F.; Giessibl, F. J.; Heinrich, A. J. *Science* **2008**, *319*, 1066−1069.
(38) Kamimura, Y.; Edagawa, K.; Iskandarov, A. M.; Osawa, M.; Umeno, Y.; Takeuchi, S. *Acta Mater.* **2018**, *148*, 355−362.
(39) Domingo-Espin, M.; Puigoriol-Forcada, J. M.; Garcia-Granada, A. A.; Llumà, J.; Borros, S.; Reyes, G. *Mater. Des.* **2015**, *83*, 670−677.
(40) Brantley, W. A. *J. Appl. Phys.* **1973**, *44*, 534−535.
(41) Wang, S. F.; Zhang, H.; Wu, X. Z.; Liu, R. P. *J. Phys.: Condens. Matter* **2010**, *22*, 055801.
(42) Errea, I.; Calandra, M.; Pickard, C. J.; Nelson, J. R.; Needs, R. J.; Li, Y. W.; Liu, H. Y.; Zhang, Y. W.; Ma, Y. M.; Mauri, F. *Nature* **2016**, *532*, 81−85.
(43) Nakashima, P. N. H.; Smith, A. E.; Etheridge, J.; Muddle, B. C. *Science* **2011**, *331*, 1583−1586.
(44) Blochl, P. E. *Phys. Rev. B: Condens. Matter Mater. Phys.* **1994**, *50*, 17953−17979.
(45) Monkhorst, H. J.; Pack, J. D. *Phys. Rev. B* **1976**, *13*, 5188−5192.

DOI: 10.1021/acs.nanolett.8b01910
Nano Lett. 2018, 18, 4611−4617